Core extraction for measuring state-to-state differential cross sections of bimolecular reactions

William R. Simpson, Andrew J. Orr-Ewing,[a] T. Peter Rakitzis, S. Alex Kandel, and Richard N. Zare
Department of Chemistry, Stanford University, Stanford, California 94305

(Received 28 April 1995; accepted 26 July 1995)

We describe a method we call core extraction for measuring the speed distributions of products from photoinitiated bimolecular reactions for the purpose of determining state-to-state differential cross sections. Core extraction is demonstrated by determination of the state-to-state differential cross section for the reaction $Cl+CH_4(\upsilon_3=1)\rightarrow HCl(\upsilon=1,\ J=1)+CH_3$. The method of core extraction measures three-dimensional projections of the velocity distribution using a time-of-flight mass spectrometer equipped with a mask to reject off-axis scattered products. This three-dimensional projection is then converted to a state-to-state differential cross section via simple transformations. Competition between instrumental resolution and signal in core extraction is discussed, and the behavior of our system is checked with simple velocity distributions that result from photodissociation of Cl_2. Core extraction is compared with other methods for the measurement of state-resolved differential cross sections. © *1995 American Institute of Physics.*

I. INTRODUCTION

Measurement of correlated product state and scattering information is one of the strongest tools for elucidating chemical reaction mechanisms. Early work used crossed molecular beam scattering methods,[1] which typically provided general pictures of the product angular distribution with some state resolution. On the other hand, chemiluminescence and laser-based techniques have offered complete state resolution but almost always lacked scattering information. A few high-resolution crossed molecular beam studies have achieved sufficient speed resolution to determine vibrational distributions along with differential cross sections. Typical of this approach are the studies of Neumark *et al.*[2] and later Faubel *et al.*,[3] who measured the correlated vibrational distribution and scattering probability in the reaction of $F+H_2\rightarrow HF+H$ and deuterated analogs. Similar techniques have been used to measure differential cross sections for the $H+H_2\rightarrow H_2+H$ and isotopically related reactions.[4,5] Rydberg tagging in conjunction with time-of-flight spectroscopy has provided extremely high resolution and revealed one of the most complete pictures of this reaction to date.[6] Ion imaging has been used to detect the complete scattering of the $H+D_2$ reaction.[7] All of these studies have inferred the product state distribution from energy conservation, which is the usual method for such work. An extension of the crossed molecular beams method that provides exact state resolution involves using lasers to effect state-selective detection in conjunction with traditional crossed molecular beams. This state-resolved method has been used with ion imaging to determine state-resolved differential cross sections for the inelastic scattering of NO by argon.[8] Beams crossing at right angles[9,10] as well as colliding head-on[11] have also been used with Doppler spectroscopy to measure state-resolved differential cross sections.

Another approach to the problem of measuring state-resolved differential cross sections involves the use of state-selective detection of the products of a photoinitiated reaction to measure both state distributions and product velocity information. This product velocity information can be inverted to the state-dependent differential cross section via center of mass to laboratory transformations. Early work on this technique was carried out by Kinsey,[12] who described an elegant Fourier transform method for inversion of Doppler profiles. Extensions of this Doppler technique have been applied to a number of inelastic scattering problems by various groups.[13–17] This method has perfect state resolution and can provide high angular resolution for favorable mass combinations. Hall and co-workers[18,19] used Monte Carlo simulation techniques to invert Doppler profiles of the OH product of the $H+O_2$ reaction to determine state-resolved differential cross sections. Aoiz *et al.*[20] derived analytical expressions for the center of mass to laboratory transformation in the presence of thermal blurring; these expressions include the effects of angular momentum polarization of the product. Brouard, Simons, and co-workers have applied this technique to numerous reactive and inelastic scattering systems, including $O(^1D)+N_2O$,[21,22] $O(^1D)+CH_4$,[23,24] and $OH+Ar/He$.[25] Casassa, King, and Sauder[26,27] used similar techniques on the $O(^1D)+H_2O$ reaction. Our group reported simpler transformations applicable when thermal blurring is not significant,[28] and we applied these methods to the reaction of Cl with vibrationally excited methane[29] and to the $H+H_2$ and isotopically related reactions.[30]

The experiments of Hall and co-workers,[18,19] Aoiz, Brouard, Simons, and co-workers,[20–25] and our experiments[28–32] all share the same underlying principle for determining state-to-state differential cross sections. We recently termed this technique of studying photoinitiated chemical reactions to determine the differential cross section the *photoloc* method.[32] This acronym stands for *photo*initiated reaction determining the differential cross section by the *law of*

[a]Present address: School of Chemistry, University of Bristol, BS8 1TS, U.K.

cosines (loc). The method is exemplified by the reaction sequence

$$AX \xrightarrow{h\nu} A+X,$$
$$A+BC \rightarrow AB(v,J)+C. \tag{1}$$

In the first step, a precursor of the reagent A is photolyzed to produce translationally excited atoms, preferably with a monoenergetic speed distribution. Because the BC molecules are stationary with respect to the AX precursor, both having been coexpanded into the vacuum system, the relative motion of A and the mass combination of the collision complex determine the magnitude of the center-of-mass velocity. These A atoms then collide and react with BC molecules to form AB molecules. The AB products are then state-selectively detected. When all other internal energies are known—the BC reagent molecule contains a known amount of internal energy and the C product carries a known amount of internal energy—conservation of energy can be applied to determine the energy available to translation for this state-selected product. This kinetic energy release determines the magnitude of the velocity of the AB product in the center-of-mass frame. The laboratory velocity of the AB product, $\mathbf{v}_{AB}$, is determined by the vector addition of the velocity of the center of mass, $\mathbf{u}$, with that of the velocity of the reaction product in the center-of-mass frame, $\mathbf{u}_{AB}$, as depicted in Fig. 1(a). The scattering angle, θ, is shown as the angle between the center-of-mass velocity and the product velocity in the center-of-mass frame. In this figure, the length of the velocity of the center of mass and the magnitude of the product velocity in the center-of-mass frame are both known by the conservation of energy considerations described above. Hence, a measurement of the product speed in the laboratory frame determines the third side of this scattering triangle and therefore all its angles, including θ, the scattering angle. Notice that the orientation of this diagram in space is irrelevant; only the magnitudes of these three velocities, $\mathbf{v}_{AB}$, $\mathbf{u}$, and $\mathbf{u}_{AB}$, are required to determine the scattering angle. For this reason, the selection of the initial reagent direction (the basis of the crossed beams method) is unimportant for measurement of the differential cross section using the photoloc method. The law of cosines relates the scattering angle to the product speed through the relation

$$v_{AB}=(v_{\mathrm{CM}}^2+u_{AB}^2+2v_{\mathrm{CM}}u_{AB}\cos\theta)^{1/2}. \tag{2}$$

This one-to-one correspondence of product laboratory speed to scattering angle is the basis of the photoloc technique.

Almost all methods to measure the speed distribution measure some laboratory-frame velocity distribution, and therefore we must also consider the angular anisotropy of the reaction products. The photolysis results in an anisotropy of the photoproduct, A, which is described by the formula

$$f(\gamma)=\frac{1+\beta_{\mathrm{phot}}P_2(\cos\gamma)}{4\pi}, \tag{3}$$

where P_2 is the second Legendre polynomial, γ is the angle of recoil of the photofragment from the linear polarization vector of the photolysing light, and β_{phot} is an asymmetry parameter that ranges from -1 to 2 and quantitatively describes the anisotropy of the angular distribution of the photoproducts. The angle γ in Eq. (3) is shown in Fig. 1(b), which also shows the laboratory frame axes used in this analysis. Because the center-of-mass direction is determined solely by the velocity of A, this asymmetry parameter also describes the angular anisotropy of the distribution of centers of mass in space. To the extent that the AB speed lies off this center-of-mass direction, the anisotropy of the product is modified. As described previously,[28] the reactive angular anisotropy is related to the reagent angular anisotropy parameter, β_{phot}, by

$$\beta_{\mathrm{eff}}=\beta_{\mathrm{phot}}P_2(\cos\alpha), \tag{4}$$

where α is the angle between the vectors $\mathbf{v}_{AB}$ and $\mathbf{v}_{\mathrm{CM}}$ and is uniquely determined for any scattering angle θ, as shown in Fig. 1(a). The angular distribution of the product is then given by substitution of β_{eff} for β_{phot} in Eq. (3). This whole discussion is predicated on the assumption of a knowledge of the energetic constraint that determines the center-of-mass frame speed of the product, u_{AB}. As shown later in this paper, the measurement of the product angular anisotropy as a function of laboratory speed can be used to check this assumption and to help determine internal energy deposition into the unobserved product, C. For the time being, we make the simplifying assumption of no energetic deposition into

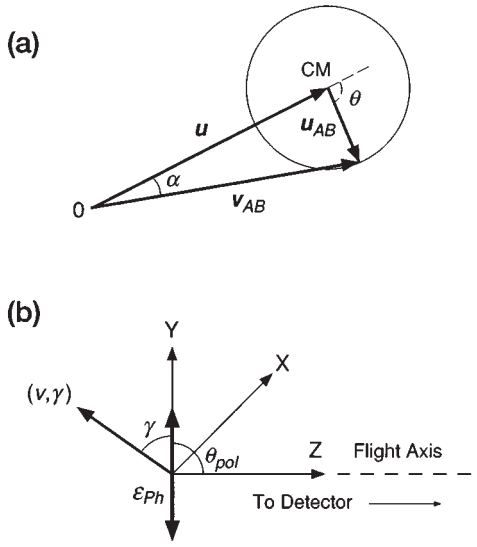

FIG. 1. Panel (a) shows the scattering triangle used by the photoloc method. The summation of the laboratory-frame vector velocity of the center of mass, $\mathbf{u}$, with the product velocity in the center-of-mass frame, $\mathbf{u}_{AB}$, to result in the laboratory-frame velocity of the product, $\mathbf{v}_{AB}$, is depicted. The scattering angle, θ, and the off-axis scattering angle, α, are also shown. Panel (b) shows the definition of laboratory-frame axes and angles used in our experiment. The Z axis is parallel to the flight axis and positive Z points toward the detector. The X axis is the axis of the horizontally propagating probe laser, and the Y axis is vertical in the laboratory frame. The thick double-headed arrow represents the polarization vector of the photolysis light, ϵ_{Ph}, which is at angle θ_{pol} from the flight axis and counterpropagates the probe laser parallel to the X axis. The spherical coordinate system used to describe the velocity distribution of the reaction products is cylindrically symmetric about the polarization vector of the photolysis light and has coordinates of speed v and polar angle γ. The arrow pointing to the coordinates (v,γ) demonstrates a direction in this space.

internal energy of the product C. With this assumption, these equations completely describe the three-dimensional velocity distribution of the reaction products. This velocity distribution is given by

$$f(v,\gamma)=\frac{1}{2v_{AB}uu_{AB}}\frac{1}{\sigma}\frac{d\sigma}{d\Omega}\left[1+\beta_{\mathrm{eff}}P_2(\cos\ \gamma)\right], \tag{5}$$

where $(1/\sigma)d\sigma/d\Omega$ is the normalized differential cross section. Equation (5) is the main result of our previous publication, Eq. (10) in Shafer *et al.*[28]

In the present paper, we transform this equation into one describing the speed distribution of the product because our resolution is fairly constant in speed. An added bonus of using the speed distribution is that it is a unique result of any photoloc experiment, even when the unobserved product consumes some of the excess energy of reaction. This point is further discussed in Sec. V. Relating the differential cross section $d\sigma/d\Omega$ to the speed distribution $d\sigma/dv_{AB}$ requires a volume element. Differentiating Eq. (2) with respect to the solid angle element Ω results in the volume element required

$$\frac{d\sigma}{d\Omega}\equiv\frac{d\sigma}{2\pi d(\cos\ \theta)}=\frac{dv_{AB}}{2\pi d(\cos\ \theta)}\frac{d\sigma}{dv_{AB}}$$

$$=\frac{uu_{AB}}{2\pi v_{AB}}\frac{d\sigma}{dv_{AB}}. \tag{6}$$

Inserting this expression into Eq. (5), we obtain the following expression for the product velocity distribution:

$$f(v,\gamma)=\frac{1}{v_{AB}^2}\frac{1}{\sigma}\frac{d\sigma}{dv_{AB}}\left[\frac{1+\beta_{\mathrm{eff}}P_2(\cos\ \gamma)}{4\pi}\right]. \tag{7}$$

Several different methods have been used or proposed for use to measure this velocity distribution. The most common is Doppler line shape analysis of reaction products using laser-induced fluorescence (LIF). Time-of-flight mass spectroscopy (TOF-MS) with resonance-enhanced multiphoton ionization has also been used in a velocity-sensitive mode to provide one-dimensional projections of the velocity distribution, which are formally equivalent to Doppler profiles.[33–40] In principle, both of these one-dimensional projection techniques provide sufficient information to determine uniquely the scattering distribution for monoenergetic reagents when no energy is deposited into the unobserved product. In actuality, speed resolution and signal-to-noise make this determination more ambiguous. Measuring the velocity distribution more directly provides a method to measure the scattering behavior with less complex analysis and less ambiguity. Shafer *et al.*[30] proposed the use of multidimensional Doppler spectroscopy to measure the velocity distribution directly. In this method, multiple lasers provide Doppler resolution along orthogonal axes to measure two-dimensional projections of the three-dimensional velocity distribution. Clearly, ion imaging could be used to measure two- or three-dimensional projections of the velocity distribution, as has been done for photodissociation experiments.[41,42] The more advanced methods of multidimensional Doppler spectroscopy and ion imaging attempt to measure velocity projections along multiple axes, as is the basis of the method presented here.

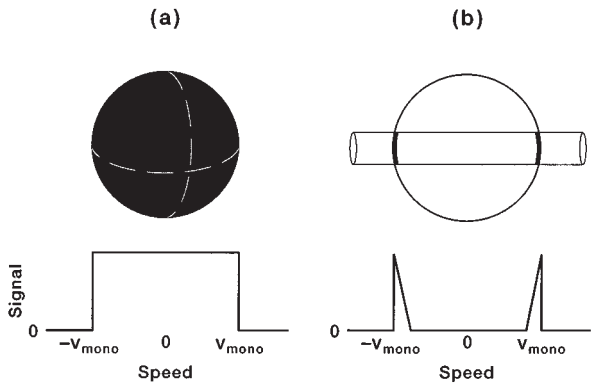

FIG. 2. Core extraction demonstrated schematically for a monoenergetic speed distribution with no spatial anisotropy. Panel (a) shows the detected ion distribution with no core extraction and the resulting signal below. Panel (b) shows the result with core extraction, where the cylinder slicing through the ion distribution represents the region of velocity space selected by the core extraction mask. The resulting signal is shown below the detected velocity distribution.

Core extraction measures the speed distribution directly by slicing the core from the velocity distribution to observe the radial layers on a linear scale. The term *core extraction* is used in analogy with the coring of an apple, in which spherical shells are observed as a linear record in the core.[43] Core extraction is an extension of the methods we have used previously to measure one-dimensional projections of the velocity distribution with a TOF-MS. In this method, a mask is placed in front of the detector to allow only ions with no speed component perpendicular to the TOF axis to hit the detector and result in signal. This technique converts a one-dimensional projection of the velocity distribution into the three-dimensional projection of the velocity distribution in which both perpendicular velocities are nearly zero. Ogorzalek Loo *et al.*[34] as well as Hwang and El-Sayed[40] used this concept with pulsed field extraction to determine kinetic energy releases in photodissociation experiments. Core extraction is formally equivalent to velocity-aligned Doppler spectroscopy (VADS)[44,45] in the case of photodissociation. VADS uses flyout induced by delayed detection with Doppler velocity resolution to effect selective detection of photofragments that have no, or only small, velocity components directed away from the detection axis. Modeling of the flyout of reaction products could be based on the core-extraction formalism in order to adapt VADS to be a probe of bimolecular chemical reactions.

The simple example of a monoenergetic speed distribution with no anisotropy and single speed, v_{mono}, is helpful in understanding the principle of core extraction. Figure 2(a) shows the density of a monoenergetic speed distribution with no anisotropy, that is, the product density in velocity space is uniformly spread on a spherical shell. The one-dimensional projection would be zero outside v_{mono} and constant at projected speeds inside the range $-v_{\mathrm{mono}}<v<v_{\mathrm{mono}}$. With core extraction, products with significant speed directed away from the TOF axis are clipped by the mask so that only products within the cylinder of Fig. 2(b) are detected. Core extraction results in an ideal signal represented by two delta

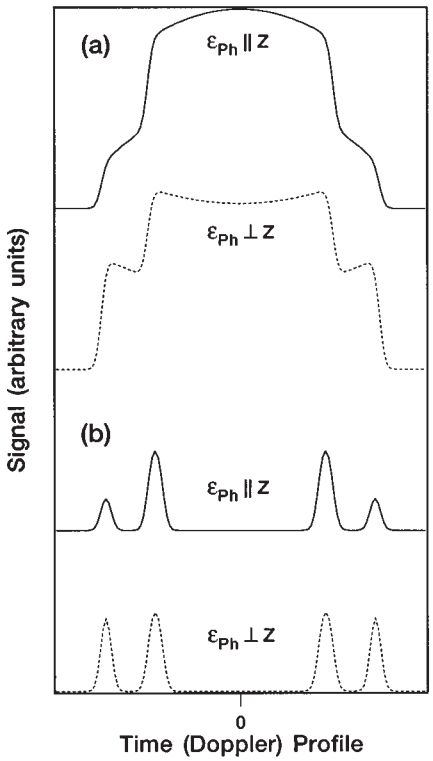

FIG. 3. Calculation of the polarization dependence of noncore-extracted and core-extracted signals for a hypothetical example. In this case, the speed distribution contains two channels. The faster channel has a perpendicular anisotropy, $\beta=-0.5$, while the slower product has no spatial anisotropy $\beta=0$. Signals are shown in two polarization geometries, the solid lines show the result for the photodissociation laser polarization parallel to the detection axis (ϵ_{Ph},$\|\mathbf{Z}$), and the dotted lines represent the result with the photodissociation laser polarization at 90° to the detection axis (ϵ_{Ph},$\perp\mathbf{Z}$). Signals are offset vertically for clarity. Panel (a) shows the simulation of a Doppler profile (or noncore-extracted time profile), and panel (b) shows the analogous core-extracted time profiles. A Gaussian width is convoluted with the signal to simulate instrument response.

functions centered at projected speeds $v=\pm v_{\mathrm{mono}}$. This change in form of the signal greatly aids in data analysis for reactive systems because without core extraction the faster products with speed projection directed off the TOF axis yield signals at the same projected speeds as slower, on-axis products. This overlap causes the fitting to be interdependent. Because products with off-axis speed components are not detected in core extraction, this method removes this source of confusion.

This advantage of core extraction is best exemplified when the scattering results in a number of laboratory speeds. Figure 3 demonstrates this simplification in form of the signal for a hypothetical example in which the speed distribution consists of two speeds, the faster speed with a perpendicular anisotropy ($\beta=-0.5$) and the slower speed with no anisotropy ($\beta=0$). The signals are calculated for the photodissociation laser polarization either parallel to the detection axis or perpendicular to the axis so that the angular anisotropy of the product can be observed. Panel (a) of this figure shows a simulation of the parallel (solid line) and perpendicular (dotted line) signals as would be recorded without core extraction. Panel (b) shows the calculated result using core extraction. Again, the solid line represents the simulation of the parallel signal and the dotted line the simulated perpendicular signal. Although the signals in both panels contain the same information, the core-extracted form demonstrates much more clearly that the speed distribution is double valued. The more advantageous aspect of the core-extracted form is visible in the polarization dependence of the signal. With core extraction, the inner channel (slower product) shows no change upon polarization switching, clearly demonstrating that it has no angular anisotropy, whereas the outer channel shows more signal in the perpendicular than parallel detection geometry. For the noncore-extracted signal, we can see that the outer (faster) channel changes form upon polarization switching and must have a negative anisotropy, but the polarization of the inner channel is affected by overlap with the faster channel. This overlap requires deconvolution that complicates the analysis and couples the uncertainty of polarization effects with the uncertainty in the speed distribution. The one-to-one mapping of the speed distribution onto signal in the case of core extraction allows more exact measurement of intensity and anisotropy by decoupling their effects and is a primary advantage of core extraction.

An experimental advantage of this selective-detection method is that only ions near the flight axis are measured, which minimizes signal distortions caused by field inhomogeneity within the mass spectrometer. For noncore-extracted signals, all ions must result in signal independent of their transverse velocity. This independence is required to measure an undistorted one-dimensional projection. Because the detector has a limited size transverse to the flight axis, it forces a limit on the size of the ion packet at the detector. The total time of flight of the ions determines both the resolution of the velocity measurement and the transverse broadening of the ion packet at the detector. Thus the requirement that all ions collide with the detector limits the experimental resolution. Because core extraction is based on the concept of rejecting some ions, this resolution limit is removed.

Core extraction also detects only products moving parallel to the flight axis, which increases the sensitivity of this technique to vector correlations between the relative velocities and angular momenta.[46] These correlations provide a more detailed picture of geometries responsible for reaction and geometries involved in the breakup of the transition state. Shafer-Ray *et al.*[32] recently reported alignment-dependent formulas for these polarization effects and we are currently analyzing our data with this formalism. Experimentally, many factors can be used to reduce or enhance these polarization effects. This paper is meant to address the technique of core extraction and leaves the additional complication of the analysis of product rotational alignment for a future publication.[47] For this reason, we have attempted to reduce product rotational-alignment effects by using weighted summation of signals in various probe polarizations to cancel approximately product rotational polarization effects. The broken cylindrical symmetry of our experiment means that no true polarization-independent spectra exist, but our combination removes the bulk of the effects. Note that without the correct co-addition of polarization-

dependent spectra, the analysis presented here is strictly correct for unaligned products of reactions of unpolarized reagents. This approximation must be recognized; that is, this treatment cannot be applied blindly to the measurement of differential cross sections without considering polarization effects.

This paper describes the method of core extraction by means of an example, the determination of the state-to-state differential cross section of the reaction $Cl+CH_4(\upsilon_3=1) \rightarrow HCl(\upsilon=1,\ J=1)+CH_3$. Following this demonstration of the method, we describe design considerations to aid other experimentalists in using the core-extraction method. The performance of the core-extraction spectrometer has been checked to demonstrate its behavior and determine the operational parameters used in determination of the differential cross section.

II. CORE-EXTRACTED TIME PROFILE ANALYSIS

The mass spectrometer is used both as a mass-sensitive detector and as a velocity-sensitive detector by exploiting the initial speed sensitivity of a linear TOF-MS.[35–40] A simple example demonstrating the speed dependence of a TOF-MS is helpful in understanding this effect. Because the ionization process does not impart significant momentum to the ion, the photoion has the same initial velocity as the neutral species of interest. Consider three ions of the same mass, one that is motionless at the time of ionization, another that moves with velocity component $|v_Z|$ toward the detector, and a third that moves with velocity component $-|v_Z|$ away from the detector. We define v_Z to be the *signed* component of **v** along the Z axis, which is taken to be parallel to the flight axis and pointing toward the detector [see Fig. 1(b)]. We define t_0 to be the time of flight of the motionless ion in our Wiley–McLaren TOF-MS.[48] The ion moving away from the detector will be stopped by the extraction field at time $|v_Z|/a$, where $a=qE/m$ is the acceleration, q is the charge on the ion, E is the extraction electric field, and m is the mass of the ion. This ion will require a small distance to stop, slightly displacing its position from the point of ionization. Because we use our mass spectrometer at space-focusing conditions, this shift in position does not affect the subsequent time of flight, and the total flight time for this ion is that for the motionless ion plus the stopping time, $t_0+|v_Z|/a$. Of course, the ion traveling initially toward the detector arrives the earliest. It behaves as if it were stopped before the ionization time by an amount $|v_Z|/a$ and was accelerated by the field to reach the velocity $|v_Z|$ at the time that ionization occurs. Hence, its arrival time is $t_0-|v_Z|/a$. When we retain the sign of this velocity component, we arrive at the expression for the total time of flight, t_{arrival}

$$t_{\text{arrival}}=t_0-v_Z/a=t_0+t_s \tag{8}$$

for the ions moving toward and those moving away from the detector. In this equation, t_s is the time shift as defined by $t_s=-v_Z/a$. Because the time shift contains all the velocity information, we plot our time profiles versus the time shift from a zero-velocity ion signal at the same mass. Using our mass spectrometer in this mode, we measure the velocity component along the flight axis from the time profile of the ion signal. This profile is then converted into velocity simply by using the known acceleration field.

The idealized core-extraction experiment is analyzed straightforwardly. Perfect core extraction results in a signal that consists of delta functions at time shifts that correspond to plus and minus the speed of the reaction product. Therefore, we obtain a one-to-one correspondence between signal in the time profile and product speed [Eq. (8)] in addition to the one-to-one correspondence between product speed and scattering angle [Eq. (2)]. Hence, we can analytically invert the time profile to a scattering distribution. In a real core-extraction experiment, ions with some width in velocity transverse to the flight axis are accepted, making the resulting time profiles broaden and start to overlap, which blurs the one-to-one correspondence between time shift and total speed. Real core extraction is more complex to analyze than ideal core extraction, but it is still simpler than no core extraction, which entails complete overlap of the slower speed signals by faster speed signals. To account for these signal overlaps and instrumental resolution, we fit the data to a linear combination of single-speed signal functions that covers the range of possible speeds for the reaction product. The coefficient of each basis function in the fit then represents the total signal at the modeled speed. This speed distribution can then be converted to a state-to-state differential cross section by the application of Eq. (6).

We call this set of single-speed signal functions the basis set or the basis vectors for the fit. As described in Sec. IV, N basis vectors are generated that are spaced equally in laboratory speed spanning the maximum speed range from the reaction. The number of basis functions used depends on the experimental resolution, and in the example of this paper, we have used 11 vectors. These vectors are chosen to be evenly spaced in laboratory speed because the experimental resolution is fairly constant in speed. Note that the nonlinearity of the conversion from speed to scattering angle implies that the angular resolution varies with scattering angle.

The basis is mathematically expressed by expanding the speed distribution in a set of monoenergetic speed functions

$$\frac{1}{\sigma}\frac{d\sigma}{dv_{AB}}=\sum_{i=1}^{N} c_i\,\delta(v_{AB}-v_i), \tag{9}$$

where v_i ($i=1$ to 11 is the index for these evenly spaced speeds) is the velocity of the basis vector. Of course this expansion is mathematically incomplete unless N goes to infinity, but because of limited experimental velocity resolution, there is a finite N at which this basis effectively spans the set of observable signals. Addition of more basis vectors simply overdetermines the problem after that point. Insertion of this form into Eq. (7) results in the following expression for the velocity distribution

$$f(v,\gamma)=\sum_{i=1}^{N} c_i\,\frac{\delta(v_{AB}-v_i)}{v_{AB}^2}\left[\frac{1+\beta_i P_2(\cos\,\gamma)}{4\pi}\right], \tag{10}$$

where the anisotropy β_t is determined by Eq. (4) for each speed v_i. Each basis vector should then correspond to the following three-dimensional velocity distribution:

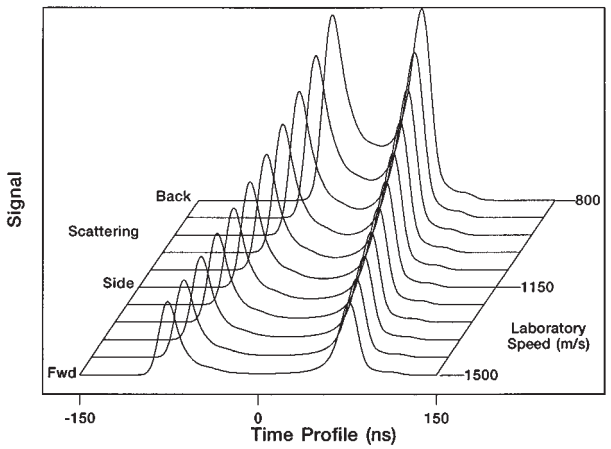

FIG. 4. The 11 core-extracted basis vectors for the reaction of atomic chlorine with vibrationally excited methane to give HCl(v=1, J=1) at an extraction field of 69 V/cm. The basis is generated for the polarization geometry in which the photodissociation laser is perpendicular to the flight axis. The axes are time-of-flight shift, velocity of the basis vector (and corresponding scattering), and signal intensity along the vertical axis. Note the independence of the basis vectors as a result of core extraction and the increased sensitivity to the slow speeds inherent in core extraction.

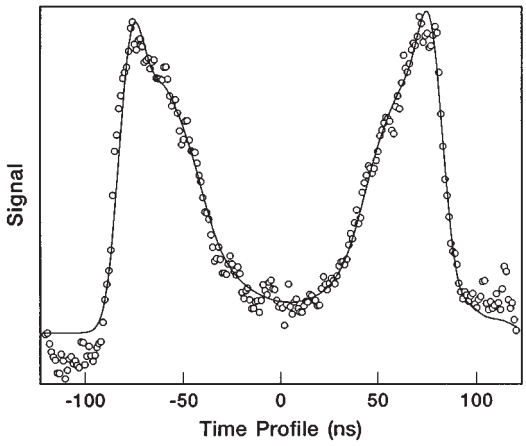

FIG. 5. Core-extracted reactive signal for HCl(v=1, J=1) from the reaction of atomic chlorine with vibrationally excited methane. See the companion paper for a description of the method used to measure this signal. The solid line represents the result of maximum-entropy fitting of the signal and the dots are the data points.

$$B_i(\nu,\gamma)=\frac{\delta(\nu_{AB}-\nu_i)}{\nu_{AB}^2}\left[\frac{1+\beta_i P_2(\cos\ \gamma)}{4\pi}\right]. \tag{11}$$

The transmission of this three-dimensional velocity distribution in a given photodissociation-polarization geometry through the core-extraction spectrometer is then calculated as described in Sec. IV. Briefly, the core-extracted signal results from conversion of Eq. (11) to Cartesian coordinates followed by integration over the off-flight-axis projections with a calculated transmission function describing the probability to detect an ion as a function of its off-flight-axis projection. The result is a signal versus on-axis speed projection, which is then converted to flight-time shift by the simple linear relationship between speed projection ν_Z and time shift t_s [Eq. (8)]. Thereby, the basis vectors $B_i(t_s)$ represent the signal as a function of time shift for this monoenergetic speed distribution. The basis is shown in Fig. 4. Because the polarization geometry in which the photolysis laser is perpendicular to the flight axis contains more information for the determination of the product speed distribution (owing to the perpendicular photodissociation of Cl_2 and kinematics of the reaction), the basis presented is for that geometry alone. The 11 basis functions are displayed versus the time shift, and the speeds of the basis vectors are marked on the plot.

The core-extracted time-of-flight signal is then given by Eq. (10) with this core extracted basis

$$f(t_s)=\sum_{i=1}^{N} c_i B_i(t_s). \tag{12}$$

After fitting the data to this form, the speed distribution is then given by the coefficients c_i substituted into Eq. (9). This linear combination can be solved by a number of methods, including least-squares fitting, singular value decomposition (SVD), or maximum-entropy fitting.[49] Because the basis set generated by core extraction is not an orthogonal set, the values of the fit coefficients are interrelated. This covariance makes a simple least-squares fit undesirable because the fit coefficients tend to oscillate to fit small noise features in the data. For this reason, we have pursued other approaches. In the past, we have used SVD fitting,[29] which creates linear combinations of the nonorthogonal basis that are orthogonal and therefore have no covariance problem. While this results in a good fit to the experimental time profiles, the calculated speed distributions sometimes predict negative populations at some speeds. To eliminate such nonphysical behavior in our models, we have chosen the maximum-entropy fitting approach described by Kim *et al.*[19] to fit the data. In this method, we use a simulated-annealing[49] least-squares fitting procedure to minimize the least-square deviation ($\chi^2=\Sigma(y-\text{fit})^2$) while maximizing the statistical entropy of the fit coefficients ($S=-\Sigma\ c_i \ln c_i$). To perform this fit, we replace the usual χ^2 figure of merit by the expression merit$=\chi^2-\alpha S$, where α is a user-selected weight. This weighting parameter is varied to achieve a smooth fit without significantly increasing the least-squares deviation of the fit (χ^2). This method allows for inclusion of the physical constraint of a positive speed distribution and produces a smooth fit when the data do not warrant spikes. The maximum-entropy procedure, however, does not allow for estimates of the error; consequently, we determine error bounds by taking the statistical error for deviations between data sets.

Core-extracted time profiles were recorded using the procedures described in the companion paper. One such time profile is included here as an example of our data-analysis technique. Figure 5 shows core-extracted data and the fit for the HCl(v=1, J=1) product of the reaction of $Cl+CH_4(\upsilon_3=1)$ at 0.159 eV collision energy. Figure 6 shows the speed distribution that is the result of this fit. The reason for first determining this speed distribution and then converting it to a scattering distribution is that the speed distribution is a direct experimental result that makes no assumptions of energy deposition in unobserved products. In a later section, this assumption is discussed, but for the time being we stay

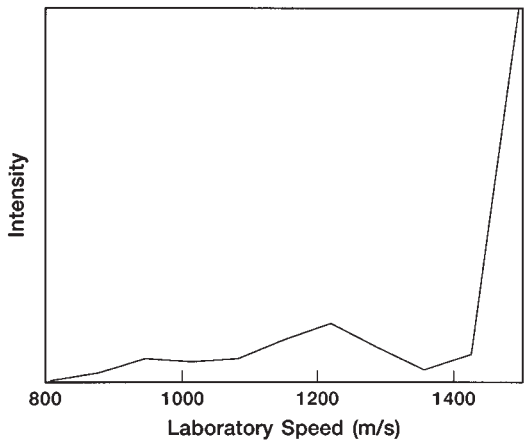

FIG. 6. The extracted speed distribution from the fit of the signal shown in Fig. 5. This figure presents the speed distribution as determined by maximum-entropy fitting of core-extracted signal and has no error estimates because it represents the best fit for that single data set.

with our assumption of full kinetic release in converting the speed distribution to the differential cross section. We need to apply the volume element correction from Eq. (6) to make this transformation. Figure 7 shows the result. This example illustrates the method of core extraction and demonstrates the simplicity of our methods for data analysis. In Sec. III, we describe experimental considerations to aid others wishing to use core extraction. In Sec. IV, we describe our methods for generation of the basis set and our checks of this basis set to demonstrate that the operation of our mass spectrometer does follow the predictions of our model. These basis set checks are important because they largely eliminate questions of systematic error in the basis set and thus prevent possible errors from propagating into error in the differential cross section.

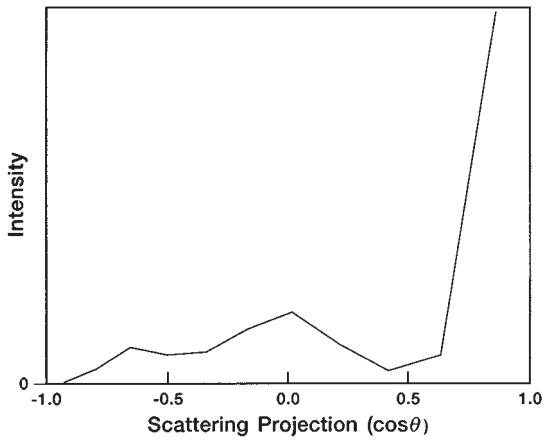

FIG. 7. The extracted state-to-state differential cross section for $Cl+CH_4(v_3=1)\rightarrow HCl(v=1,\ J=1)+CH_3$. Again, no error estimates are shown because the result represents the best fit for the single data set shown in Fig. 5. This figure assumes no internal excitation of the methyl radical in order to convert the speed distribution to a scattering distribution.

III. DESIGN PARAMETERS FOR A CORE-EXTRACTION SPECTROMETER

When using core extraction, particularly when investigating low-signal systems such as chemical reactions, consider the trade-off between need for signal and effective core extraction. This trade-off can be balanced in two ways: (1) the voltages used in the mass spectrometer can be changed, effectively changing the degree of core extraction by changing the size of the ion image at the core extractor; and (2) the size of the core extractor can be varied. In our setup, the size of the extractor is fixed, and only the voltages can be changed. The signal into a unit of time scales roughly as E^2, where E is the extraction electric field. Increasing the extraction field by a factor of two will increase the signal by a factor of 4. For this reason, we have used a variety of voltage conditions in our experiments depending on the strength of the signal. With our fixed-size core extractor, both of these effects are inherently coupled by the Wiley–McLaren space-focusing relationship. A system that allows variation of the size of the core extractor could decouple these effects. To use the simple relationship between time-of-flight shift and product velocity, Eq. (8), a linear time-of-flight mass spectrometer must be used at Wiley–McLaren space-focusing conditions.[48] Of course, other voltage conditions could be used, but a more complex relationship would be necessary to invert the measured time profile to a speed distribution.

The most important part of the design of a core extraction mass spectrometer is that which maintains a separation of the transverse speed components from the longitudinal components. The separation of speed components is achieved by ensuring that all fields are homogeneous and point parallel to the flight axis. Failure to maintain separation between field components causes the off-axis speed components to mix into the longitudinal speed component, changing the time of flight. Also, any field mixing acts as a lens that reshapes the expanding ion cloud such that an ion's spatial displacement from the ion cloud center no longer indicates the ion's transverse speed component. Field homogeneity was achieved through the use of oversized extraction electrodes along with field shimming electrodes, as described in the companion paper. Alignment of the ion optics by retroreflecting a He–Ne laser off a mirror temporarily placed on each of the optics allowed all electrodes to be made perpendicular to the flight axis, therefore creating parallel electric fields. The field homogeneity and Wiley–McLaren space-focusing condition can be optimized by measuring the time-of-flight shift of a laser-ionized peak from an initially motionless sample as the probe laser beam is translated within the extraction region. A well-optimized spectrometer operating at space-focusing conditions should show a trivially small dependence of the time of flight on the probe laser beam position. We also used pulsed steering, as described in the accompanying paper, to steer the ions without fringe field lensing. With these precautions, we found that the simple model for the core-extraction process described in Sec. IV was able to accurately predict experimentally observed time profiles from monoenergetic speed distributions.

IV. BASIS SET GENERATION

Modeling of ion transmissions for monoenergetic product speed distributions through the core-extraction mass spectrometer results in the basis set for the fitting procedure. The expansion of the ion cloud is caused solely by its initial velocity distribution in the dimensions perpendicular to the flight axis. We define the initial velocity distribution to be measured in a Cartesian basis as $f(\nu_X,\nu_Y,\nu_Z)$. Our choice of coordinates takes positive Z to be pointing toward the detector along the flight axis, X to be the probe laser beam propagation direction (horizontal in the laboratory), and Y to be the vertical axis. In the limit of perfect core extraction, only ions with $\nu_X=\nu_Y=0$ will be detected, and the resulting time profile will be $f(0,0,\nu_Z)$. Of course, perfect core extraction eliminates most ions, and a trade-off exists between effective core extraction and signal. As the core extractor is made larger, ions with some width of velocities along X and Y will also hit the detector. Therefore, the core-extracted signal is calculated as the product of the detection probability along ν_X and ν_Y times the signal at that ν_X, ν_Y, and ν_Z. The basis vectors are the result of modeling core extraction for the three-dimensional velocity distribution described by Eq. (11). We rotate this distribution from the frame of the polarization vector to that of the flight axis, then transform it into Cartesian coordinates to generate $f(\nu_X,\nu_Y,\nu_Z;\nu_i,\beta_i,\theta_{\rm pol})$, where $\theta_{\rm pol}$ is the angle of rotation between the photolysis frame and the flight axis [see Fig. 1(b)]. This function is a Cartesian three-dimensional velocity distribution in which the variables of the function are listed before the semicolon, and the parameters are listed after the semicolon. In the discussion below, we model the transmission of this velocity distribution through our apparatus.

We begin with the assumption that all ions form on a line along the X axis (the probe laser axis). These ions then fly through the slit to the core extractor in a time that is calculated in Sec. II, t_0+t_s. The vertical position of an ion packet at the core extractor is then $\nu_Y(t_0+t_s)$. The reaction and detection chambers are separated by a defining slit designed to cut a small packet of ions from the long line of ions formed along the Rayleigh range of the focused ionization laser. This ion packet clipping was necessary to define an initial X position for the ions so the core extractor can spatially reject ions with $\nu_X\neq 0$. From an initial X position in the slit, X_i, we calculate the horizontal offset of the ion packet at the core extractor as $X_i+\nu_X t_{\rm sce}$, where $t_{\rm sce}$ is the time from the slit to the core extractor. Note that in our technique, all the separation caused by the initial velocity occurs in the source region; therefore, the time from the slit to the core extractor is not dependent on the initial longitudinal velocity, and the horizontal offset after the slit is $\nu_X t_{\rm sce}$. We can then calculate the radial offset of an ion packet from the center of the core extractor $\rho(\nu_X,\nu_Y,X_i)$ based on the vector summation of these X and Y offsets.

The transmission function of the core extractor $T(\rho)$ represents the probability that an ion goes through the circular core extractor and results in signal as a function of ρ, the radial offset of the ion from the center of the core extractor. Calculation of $T(\rho)$ is described later. Because our probe laser has some Doppler resolution, we do not ionize the whole velocity distribution uniformly but instead have a probability $D(\nu_X)$ to ionize a product with ν_X velocity projection along the probe laser direction. In our case, power broadening makes this detection function a Lorentzian with a FWHM of approximately 3000 m/s. Hence, the core-extracted signal is the integral over all ν_Y and ν_X, and slit position X_i, of the radial transmission times the Doppler selection times the intensity at that ν_X,ν_Y,ν_Z. This intensity as a function of ν_Z is converted to a time shift by the relation $t_s=-\nu_Z/a$. This signal represents the core extracted signal in the absence of any instrumental resolution blurring.

Instrumental resolution has two effects on the core-extracted signal. First, blurring of velocities along the flight axis adds some temporal width to the observed time profile. Second, blurring of velocities transverse to the axis degrades the core extraction. These blurrings can come from a number of sources including residual thermal motion in our jet-cooled sample, the spread of ionization times caused by the laser pulse width, elastic collisions of the ions, inhomogeneity of fields, and imperfections in instrument alignment. We approach this problem by adding longitudinal and transverse instrumental resolution to our calculation and varying the resolution parameters to fit a wide range of experimental monoenergetic speed distributions. Studies in which the ion yield was varied showed no discernable effects from Coulomb repulsion of the ions. Hence, we believe that Coulomb repulsion was an insignificant source of blurring.

Time-delay studies showed that after we made a small correction for flyout of the faster reaction products from the probe volume, the reactive time profile was independent of reaction time. Therefore, translational relaxation of the product before ionization was also not the cause of the blurring. The flyout correction was made by approximating the density of chlorine atoms as Gaussian at the size of our photolysis beam at the time of the photolysis and integrating the rate equation for the density of products as a function of velocity component along the flight axis over the reaction time. This treatment resulted in a detection probability that depends on the velocity of the product and the time of reaction. This correction was applied to the experimental data by dividing the core-extracted signal by the calculated detection probability to generate flyout-free time profiles. The correction was maximally 30% across the range of possible speeds from the reaction of $Cl+CH_4(v_3=1)$.

Transverse blurring is included by calculating the overlap of a spatially blurred ion packet with the core extractor as a function of the distance between the center of the ion packet and the core extractor. This calculation results in the transmission function $T(\rho)$ mentioned above. We have used the arbitrary form for the blurring, $I(r)=\exp(-r/w)$, where r is the radial distance from the center of the packet, $w=\mathrm{FWHM}/2(\ln 2)$, and FWHM is a variable parameter. The full width varied with extraction voltage. The parameters used to model the data are shown in Table I. Longitudinal blurring is included by convolution of the modeled signal with an instrument function that consists of a Gaussian function followed in time by two smaller Gaussian rings (6% and 4% of the original signal at 18 and 36 ns delay) of the same width that was included to model the electronic ringing of

TABLE I. Operating conditions and experimental resolution used in modeling Cl atom signals.

Extraction field (V/cm)	Longitudinal blurring (ns)[a]	Transverse blurring (mm)[b]	Relative signal[c]	Resolution (m/s)[d]
69	9	2	≡1	170
113	8	1.5	2.7	250
169	7	1	6.1	320

[a]Full width at half maximum of the Gaussian function describing the instrument time response function.
[b]Full width at half maximum of the ion packet transverse blurring as described in text.
[c]Signal relative to 69 V/cm extraction field using the approximate scaling described in the text. Note that this is an upper bound for the signal increase, and the actual relative signal increase will be smaller because of the fact that core extraction goes over to integral ion collection as the field is increased.
[d]Resolution as defined by the equivalent speed of the full width at half maximum of the instrumental function.

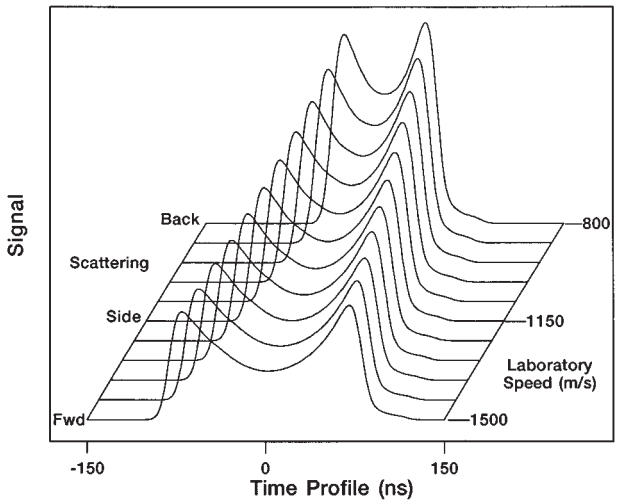

FIG. 8. The noncore-extracted basis for the reaction of $Cl+CH_4(\upsilon_3=1)\rightarrow HCl(\upsilon=1, J=1)+CH_3$. The axes are the same as in Fig. 4. Note how the basis has complete overlap of slow basis functions by faster, more forward scattered, basis vectors.

our detection system. The reactive data show clearly that more blurring occurs than for Cl atom profiles. We believe the origin of this effect is deviation from the assumption of zero temperature of the target gas. Because our target gas is much lighter than Cl_2, we would expect to see this effect only when observing reactive signal and not when recording time profiles of Cl atoms. We have included this blurring contribution in our fits by increasing the longitudinal blurring to 13 ns for reactive time profiles at 69 V/cm. Deconvoluting this width from the 9 ns instrumental function, we find approximately 150 m/s FWHM of blurring. If we assume that this blurring is caused by the thermal motion of the methane molecules, we can derive an equivalent temperature of approximately 15 K.

We note that the core-extracted basis is biased toward backscattered product because the slower signals are less effectively rejected by the core extractor. Experimentally, the backscattered product also has a large sensitivity to steering error of the ions. This steering error could result from the experimental error whereby the ion image is incorrectly centered on the core extractor. The error makes a larger change for the slower speed products because they are being less effectively rejected by the core extractor and therefore have a greater sensitivity to the nature of the process of core extraction. In our experiments, we set the steering by maximizing signal on a zero-velocity sample of HCl contaminant. This procedure should center the ion image on the core extractor, but we are still subject to a greater possibility of systematic error in this part of the speed distribution. We attempted to include this error in our statistical error bounds by carrying out the experiment on multiple days with possibly different steering conditions and comparing our results. Despite this difficulty in experimental optimization, we have found that careful application of the core extraction method results in reliable measurements of the speed distribution for the purpose of state-to-state differential cross section measurements.

The core-extraction technique differs from Doppler profile measurements because our technique is sensitive only to products with little or no off-axis components of their velocity along the flight axis. To compare core extraction to the Doppler profile method, we show in Fig. 8 the basis set that would result without core extraction, which assumes all ions are detected uniformly independent of their transverse velocity. This calculation results in a one-dimensional projection of the three-dimensional velocity distribution, which is formally equivalent to a Doppler profile. As can be clearly seen in Fig. 8, the functions overlap, so the backscattered signals overlap signal at the same time-of-flight shift by faster, forward-scattered products. The core-extracted basis shown in Fig. 4 reduces this problem by decreasing the signal overlap. Core extraction also removes the limitation that the detector is sufficiently large to capture all ions independent of their transverse velocity.

Instrumental basis functions generated by the method described above were fit to a number of monoenergetic speed distributions. The shape of the time profiles, the ratio of signals as a function of angle of the photolysis polarization from the flight axis, and the ratio of core-extracted to noncore-extracted signals were all effectively fit by the procedure described above. The speeds and anisotropies for photolysis of Cl_2 as a function of wavelength are well known[50,51] and are summarized in Table II.

Figure 9(a) shows the core-extracted time profile of ground-state Cl $^2P_{3/2}$ atoms from 355 nm photolysis of Cl_2 with the photolysis laser both approximately parallel (8°) to and perpendicular (98°) to the flight axis.[52] The modeling

TABLE II. Photolysis parameters of Cl_2 (Refs. 50,51).

Detected atom	Photolysis wavelength	Speed[a]	Anisotropy
Cl $^2P_{3/2}$	355 nm	1677 m/s	−1
Cl $^2P_{1/2}$	355 nm	1577 m/s	+2
Cl $^2P_{1/2}$	416 nm	1039 m/s	+2

[a]For mass ^{35}Cl atom. The reported speed is the average speed taking into account the possibility of photolysis of both $^{35}Cl_2$ (75%) and $^{35}Cl^{37}Cl$ (25%), which differ in speed by a few percent.

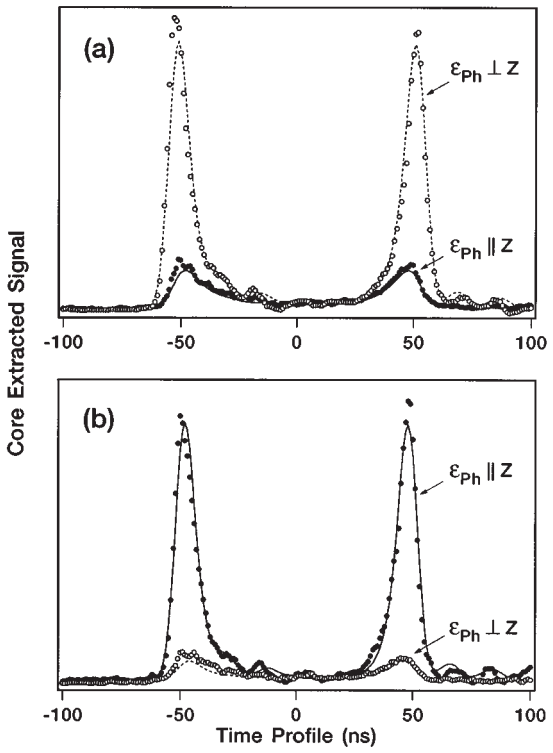

FIG. 9. Polarization-dependent time profiles of ^{35}Cl atoms from the photodissociation of Cl_2 at 355 nm with core extraction at an extraction field of 113 V/cm. Panel (a) depicts the ground state Cl $^2P_{3/2}$ atoms; the solid line and filled dots are the fit and signal, respectively, for polarization of the photolysis parallel (8°) to the flight axis. The dashed line and open symbols are fit and signal, respectively, with the photolysis polarization perpendicular (98°) to the flight axis. The experimental data are recorded using the photoelastic modulator to flip the polarization of the photolysis beam on every other shot, and their relative intensities represents that caused by the anisotropy of the photodissociation. Similarly, the relative intensities of the fit are taken from the model and are not independently normalized. Panel (b) shows the result for spin–orbit-excited Cl $^2P_{1/2}$ atoms from the photodissociation of Cl_2 at 355 nm. Experimental conditions and labeling of curves are as in panel (a). Note that the polarization of the spin–orbit-excited Cl $^2P_{1/2}$ atoms is opposite to that of the Cl atoms at the same wavelength, as readily observed by the increase in parallel signal over perpendicular signal.

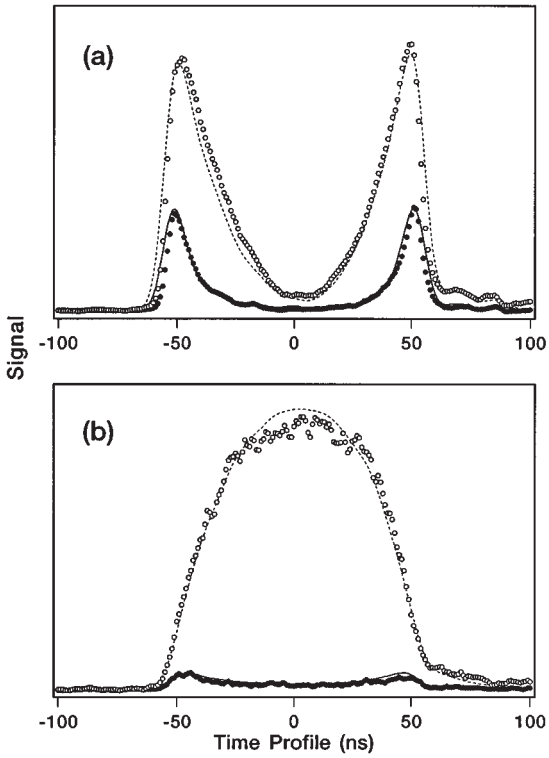

FIG. 10. The effect of core extraction on the time profiles of spin–orbit-excited ^{35}Cl $^2P_{1/2}$ atoms from the photodissociation of Cl_2 at 416 nm with core extraction at an extraction field of 69 V/cm. Panel (a) shows the result with the polarization of the photodissociation parallel to the flight axis. The dashed line and open symbols are the fit and signal, respectively, for signal with no core extraction. The solid line and filled dots are fit and signal with core extraction. The experimental data were taken in successive scans and are absolutely scaled. Therefore, the relative intensities represent those caused by the rejection of the core extractor. Similarly, the relative intensities of the fit are taken from the model and are not independently normalized. Note that the voltage conditions are different from that of Fig. 9, and these slower Cl $^2P_{1/2}$ atoms coincidentally have a similar time splitting between peaks. Panel (b) show the result when the polarization of the photodissociation is perpendicular to the flight axis. Experimental conditions and labeling of curves are as in panel (a). Note that even though the core extractor rejects nearly all the ions in this geometry, the model still is able to reproduce the core-extraction ratio and shape of the signal.

replicates the features of the signal and the absolute ratio of nearly parallel to nearly perpendicular signal for this photodissociation. This fit also demonstrates our method's sensitivity to the angular anisotropy of the products in space. Figure 9(b) shows the same plot, but for spin–orbit-excited Cl $^2P_{1/2}$ atoms at 355 nm. Because the anisotropy is at the other extreme from the ground-state Cl $^2P_{3/2}$ atoms, we see that the nearly parallel (8°) signal is larger.

To verify that our modeling works for a range of velocities, we performed experiments at a lower photolysis energy to generate slower spin–orbit-excited Cl $^2P_{1/2}$ atoms. These Cl $^2P_{1/2}$ atoms are moving slower than the center of mass of the reactive system, while ground-state Cl $^2P_{3/2}$ atoms at 355 nm move faster than the fastest possible HCl(v=1, J=1) product. Figure 10(a) shows time profiles for spin–orbit-excited Cl $^2P_{1/2}$ atoms at a lower voltage condition (higher resolution) than Fig. 9 with both core-extracted signal and noncore-extracted signal and with the photodissociation laser parallel to the flight axis. The noncore-extracted signal is modeled by taking the size of the core extractor to be that of the microchannel plates. The shape of the core-extracted signal and the fraction of detected ions are represented well by the modeling. This same test is repeated in panel (b) for the case in which the photolysis polarization is perpendicular to the flight axis. Again, agreement is good.

One last check on the validity of the modeling is performed by measuring the ratio of core-extracted to integral signal for a nominally motionless sample of HCl. Here, jet-cooled HCl is ionized, and the core-extraction ratio is measured. Typically, at an extraction field of 69 V/cm, we obtain experimentally 0.6 ± 0.1, whereas our model gives 0.65.

V. ESTIMATION OF INTERNAL ENERGY RELEASE

Figure 11(a) shows the kinematics and energetics of the reaction of $Cl + CH_4(v_3=1) \rightarrow HCl(v=1,\ J=1) + CH_3$. Panel (a) represents a velocity–space Newton diagram adapted for use in a photoinitiated reaction. The vertex on the left side

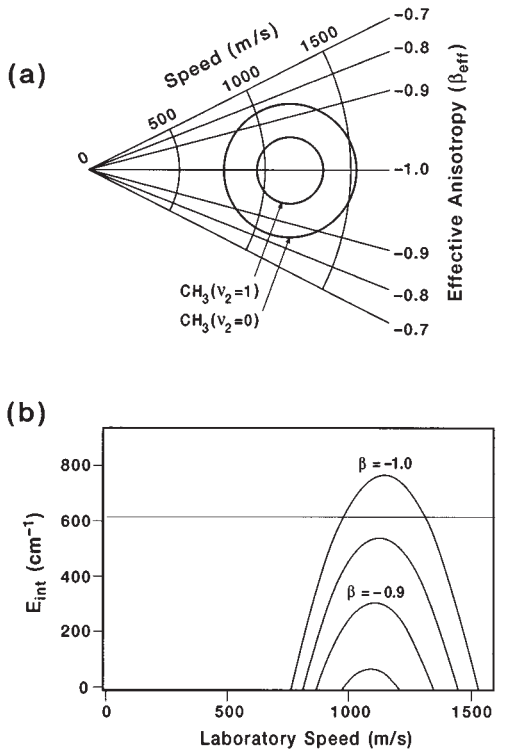

FIG. 11. Two methods are presented to relate the spatial anisotropy of the HCl(v=1, J=1) product of the photoinitiated reaction of Cl+CH_4(υ_3=1) to internal energy deposition into the unobserved product (CH_3). Panel (a) shows the velocity–space Newton diagram adapted for a photoinitiated reaction with two Newton rings, one for vibrationless methyl (υ_2=0) and one for one quantum of methyl umbrella mode excitation (υ_2=1). Panel (b) shows the energetic viewpoint for this same reaction. Curves of constant beta parameter are plotted versus observed laboratory speed of the HCl product. The thin horizontal line is drawn at the energy of the first quantum of methyl umbrella mode vibrational excitation. See the text for further detail.

represents the origin of speed in the laboratory, that is, the laboratory zero of speed. Directly to the right from this point, we see the speed of the center of mass of the system (at 1150 m/s). Based on the amount of internal energy carried by the unobserved product, the methyl radical in this case, we calculate the speed of the HCl(v=1, J=1) product associated with this internal excitation in the center-of-mass frame. This speed constrains this product to a Newton circle about the center of mass. The diagram shows two such Newton circles, one for no methyl excitation, and one for one quantum of ν_2 umbrella mode excitation. The vector summation of product velocity in the center-of-mass frame with the center-of-mass velocity gives the laboratory velocity of the product. In the photoloc method, the magnitude of the product velocity is what is primarily measured. In Fig. 11(a), the product speed is represented by the arcs concentric on the laboratory origin labeled with laboratory speed. The disadvantage of using photoloc for measurement of the differential cross section in polyatomic reactions is that some ambiguity arises as to the internal energy deposited into the unobserved product. For example, at 1000 m/s, both the CH_3 υ_2=0 and υ_2=1 Newton circles intercept that laboratory speed arc. Therefore, signal observed at 1000 m/s in the laboratory could either be backscattered HCl with $CH_3(\upsilon_2=1)$ or side-scattered HCl with $CH_3(\upsilon_2=0)$.

If the angular distribution of reagent Cl atoms in space were isotropic, there would be no way to know which of these cases had occurred. The off-axis component of the scattering is different for these two examples, however, and this off-axis nature modifies the anisotropy of the HCl product in space. This condition is mathematically expressed by the relation between α and $\beta_{\rm eff}$ expressed in Eq. (4). In Fig. 11(a), the angle α corresponds to the angle between a HCl product direction and the horizontal line. Because the physically observable quantity in a photoinitiated reaction is the product anisotropy, $\beta_{\rm eff}$, lines of constant $\beta_{\rm eff}$ are used as the angular coordinates of this figure. Returning to our 1000 m/s example, we see that the figure predicts an anisotropy of $\beta_{\rm eff}=-1$ for HCl associated with umbrella excited methyl and $\beta_{\rm eff}=-0.85$ for HCl associated with ground state methyl. Therefore, we can in principle determine properties of the unobserved internal energy deposition by observing the anisotropy of the product. Unfortunately, the anisotropy is the average of all products at the same laboratory speed. This averaging means that only the average off-axis nature is observed, which is invertable to a mean energy deposition and has no possibility to determine the form of the distribution. This disadvantage is inherent in the method of differential cross section measurement via a photoinitiated reaction and requires a more complex experiment to resolve the ambiguity. Additionally, in this case, the anisotropy varies maximally by about 15%, which is too small to be observed with the present signal-to-noise ratio. In more favorable kinematic cases (center-of-mass product speeds nearly equal to the center-of-mass speed), this anisotropy measurement is capable of determining the off-axis nature more reliably (see companion paper). Figure 11(b) shows this same reaction cast in an energetic framework instead of a velocity framework. For many cases, the possible internal energy states of the unobserved product will form a pseudocontinuum, and this approach will be preferable.

Both of these panels demonstrate how the experimentally observable product anisotropy is related to the internal excitation of the unobserved product. Experimentally, measurement of the product angular anisotropy is achieved by rotating the polarization of the photodissociation laser beam. To achieve the best fit to the polarization-dependent data, the input anisotropy parameters are varied iteratively. This procedure results in β_i and c_i for each basis vector i, associated with speed ν_i. This beta parameter is then converted into a product speed release using the scattering triangle shown in Fig. 1 and the relationship between $\beta_{\rm eff}$ and α given in Eq. (4) to yield u_{AB_i} for vector i, specifically,

$$u_{AB}=(\nu_{\rm CM}^2+\nu_{AB}^2-2\nu_{\rm CM}\nu_{AB}\cos\alpha)^{1/2}$$
$$=\left(\nu_{\rm CM}^2+\nu_{AB}^2-2\nu_{\rm CM}\nu_{AB}\left(\frac{2\beta_{\rm eff}/\beta_{\rm phot}+1}{3}\right)^{1/2}\right)^{1/2}. \quad (13)$$

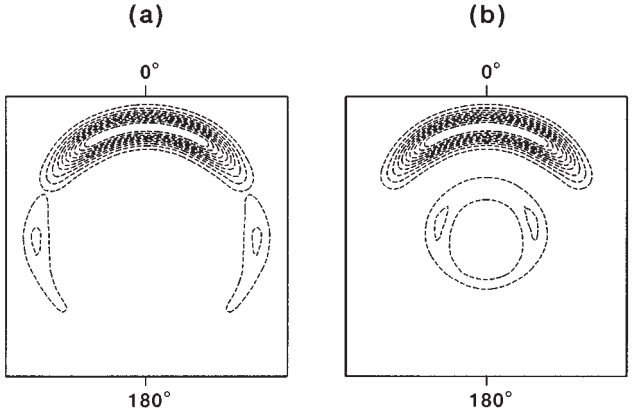

FIG. 12. Contour plots of two possible scattering distributions consistent with our measured speed distribution shown in Fig. 6. The plots represent the scattering probability in contours versus the two dimensions representing the center-of-mass frame scattering speeds of the HCl ($v=1$, $J=1$) with methyl excitation. The center of the plot is the center of mass and upward on the page is forward scattered (shown as 0°). If the methyl were not vibrationally excited, distribution (a) would be the only possible distribution of HCl speeds in the center of mass. Distribution (b) represents the maximal excitation of methyl umbrella bending that is consistent with our speed distribution. The removal of energy from translation to internal energy of the methyl requires that the product moves more slowly away from the center of mass, and therefore the large forward-scattered peak is moving too fast to have been formed in coincidence with methyl excitation.

To obtain the differential cross section, we need to apply the volume element correction described by Eq. (6). We can then plot the data in either of two ways. We can plot a Newton diagram with the differential cross section describing the intensity at angle θ and u_{AB} for the radius. Alternatively, we can make plots of $\partial\sigma/\partial\cos\theta$ and $\langle E_{\rm int}\rangle$ as a function of scattering angle. The Newton diagram approach can be misleading because it places all the intensity at radius u_{AB}, where there may not even be a possible state. This erroneous location of intensity results from the averaged nature of the anisotropy parameter; it can be corrected by assuming a form for the distribution of unobserved states populated and creating a Newton diagram using these allowed state energies and populations subject to the constraint that the average u_{AB} is matched. An advantage of reporting only the average of the internal energy deposition is that it does not require any assumption about the form of the internal energy distribution.

As mentioned before, the example presented here has no additional anisotropy constraint owing to the nature of the mass combination and energetics of this product state. For this reason, we generate Newton diagrams with the maximal and minimal methyl excitation to visualize the level of ambiguity in our inversion. Figure 12 shows Newton diagrams for two possible scatterings in which the methyl umbrella vibration is constrained to be in $v_2=0$ or 1. Both scattering distributions are consistent with the measured speed distribution and differ simply in the amount of methyl excitation. Figure 12(a) shows the result for no methyl excitation, and Fig. 12(b) shows the result with maximal methyl excitation consistent with our data. As can be seen, the overall features of the scattering, specifically the large forward peak and lack of backscattering, are not very dependent on the selection of methyl population distribution. Hence, we conclude that our speed measurement provides a general picture of the reactive scattering process.[53]

VI. DISCUSSION AND CONCLUSIONS

Photoinitiated bimolecular reactions in which the reagent collision energy is controlled and the internal state of the product is selected can provide a simple, high-signal method to measure state-resolved differential cross sections, the routine observation of which has been a major goal of experimental studies of reaction dynamics for many years. In this technique, which we call the photoloc method, the differential cross section is deduced from a measurement of the velocity distribution of the state-selected product via the law of cosines which relates the three sides of a triangle (the speed of the center of mass, the speed of the state-selected product in the center-of-mass frame, and the speed of the state-selected product in the laboratory) to the angles of the triangle, specifically, to the scattering angle. In these experiments, the product molecule is detected in a state-selective manner by resonance-enhanced multiphoton ionization (REMPI). We have described a special method called core extraction for determining the velocity distribution of the state-selected product molecules in the laboratory frame. In core extraction a mask is placed in front of the detector of a standard linear time-of-flight mass spectrometer to record directly the speed distribution of the product ions moving on axis. Although the combination of the photoloc method with core extraction lacks complete generality because of the need to find suitable precursors that produce upon photolysis single-speed reagents and the need to find suitable products that are easily detected by REMPI, many reaction systems meet these conditions. For these photoinitiated reactions, the photoloc method combined with core extraction provides a powerful technique for the measurement of state-resolved and state-to-state differential cross sections.

Core extraction has distinct advantages compared to Doppler spectroscopy for measurement of speed distributions. These benefits include resolution enhancements, increased orthogonality in the relation between the differential cross section and the observed signal, and several technical improvements. Additionally, core extraction has the advantage that the form of the differential cross section is visible directly in the experimental data. For instance, the core-extracted signal from a forward-backward scattered reaction would consist of two double-peaked signals centered about plus and minus the center-of-mass speed, whereas the Doppler-resolved form has a ''wedding cake'' appearance [contrast Fig. 3(a) with Fig. 3(b)]. The core-extraction method is fairly simple to implement in a standard design time-of-flight mass spectrometer. In core extraction, signal magnitude, and resolution are inversely related. Therefore, selection of operating voltages allows an experimental resolution to be chosen based on the signal level of the reaction being investigated, as discussed.

In the reaction of atomic chlorine with vibrationally excited methane, the core-extraction method has significantly improved our resolution of the center-of-mass differential cross section. Just as in the method of crossed molecular beams, the conversion between the experimental observables and the differential cross section is nonlinear, which causes the resolution to vary with the scattering angle. For this kinematically unfavorable case, our resolution is nearly constant in the scattering projection, $\cos\theta$, and is $\Delta\cos\theta \approx 0.3$. This resolution corresponds to a center-of-mass resolution of approximately 45° in the forward- and backscattered regions and 20° in the side-scattered region. For reactions involving better mass and exothermicity combinations, this resolution is improved (see Shafer *et al.*[28] for a discussion), and of course, detection with better speed resolution also improves this angular resolution.

Analysis methods for conversion of observed time profiles to speed distributions have been presented. Our analysis method is preferable to forward-convolution methods because it uses a direct inversion of the experimental data by maximum-entropy fitting. This procedure requires the generation of a basis set of simulated time profiles for single-speed products, which we have generated by a simulation of our experimental system. Comparison of simulated time profiles with experimental time profiles from monoenergetic speed distributions produced by photodissociation of molecular chlorine checked the basis set generation procedure. This check demonstrates the performance of our simulation method and reduces the possibility of error in this part of the analysis.

Core-extracted polarization measurements also allow for estimation of the energetic deposition into the unobserved product formed in coincidence with each detected product state. The velocity selectivity of core extraction improves the sensitivity to these polarization measurements by decoupling the spatial anisotropy of the reaction product from the speed distribution. The state-independent detection traditionally used in the method of crossed molecular beams resolves the product kinetic energy release but not the fraction of internal energy appearing in either of the products. For a reaction yielding two polyatomic products, such as the reaction studied in this paper, this lack of determination of the energetic fractionation may lead to ambiguity in the determination of the product state distributions. For example, a traditional crossed beam investigation of the reaction of Cl with CH_4 would determine the distribution of product internal energies but could not directly determine whether the HCl or CH_3 product contains that internal energy. The resolution demonstrated in this and the following paper is similar to that of many crossed molecular beam studies. Additionally, the unambiguous determination of the product state associated with each differential cross section goes far beyond most traditional studies.

Moreover, the velocity-selective detection used in the core-extraction method allows measurement of vector correlations by using polarized lasers for excitation and detection. Vector correlations measure the dependence of the reaction on vector properties of the reagents or measure vector properties of the products. For example, in the following paper, we determine the probability of reaction as a function of the angle between the approach of the reagents and the vibrationally excited C–H bond. Through the technique of core extraction, we are able to gain a much more detailed understanding of the reactivity of atomic chlorine with vibrationally excited methane. The observation of this mechanistic detail is the subject of the following paper.

ACKNOWLEDGMENTS

S.A.K. and W.R.S. thank the National Science Foundation for predoctoral fellowships. This work has been supported by the National Science Foundation under Grant No. CHE-93-22690.

[1] R. D. Levine and R. B. Bernstien, *Molecular Reaction Dynamics and Chemical Reactivity* (Oxford University, New York, 1987).
[2] D. M. Neumark, A. M. Wodtke, G. N. Robinson, C. C. Hayden, and Y. T. Lee, J. Chem. Phys. **82**, 3045 (1985).
[3] M. Faubel, B. Martinez-Haya, L. Y. Rusin, U. Tappe, and J. P. Toennies, Chem. Phys. Lett. **232**, 197 (1995).
[4] S. A. Buntin, C. F. Giese, and W. R. Gentry, Chem. Phys. Lett. **168**, 513 (1990).
[5] R. E. Continetti, B. A. Balko, and Y. T. Lee, J. Chem. Phys. **93**, 5719 (1990).
[6] L. Schnieder and K. Welge, in *Proceedings of XIVth International Symposium on Molecular Beams*, Berkeley, 1992 (Lawrence Berkeley Lab. Berkeley, 1992), p. 27.
[7] T. N. Kitsopoulos, M. Buntine, D. P. Baldwin, R. N. Zare, and D. W. Chandler, Science **260**, 1605 (1993).
[8] A. G. Suits, L. S. Bontuyan, P. L. Houston, and B. J. Whitaker, J. Chem. Phys. **96**, 8618 (1992).
[9] B. Girard, N. Billy, G. Douedard, and J. Vigúe, J. Chem. Phys. **95**, 4056 (1991).
[10] A. G. Suits, P. De Pujo, O. Sublemontier, J. P. Visticot, J. Berlande, J. Cuvellier, T. Gustavsson, J. M. Mestdagh, P. Meynadier, and Y. T. Lee, Phys. Rev. Lett. **67**, 3070 (1991).
[11] H. Meyer, J. Phys. Chem. **99**, 1101 (1995).
[12] J. L. Kinsey, J. Chem. Phys. **66**, 2560 (1977).
[13] J. Park, N. Shafer, and R. Bersohn, J. Chem. Phys. **91**, 7861 (1989).
[14] J. F. Hershberger, S. A. Hewitt, S. K. Sarkar, G. W. Flynn, and R. E. Weston, Jr., J. Chem. Phys. **91**, 4636 (1989).
[15] G. W. Johnston, S. Satyapal, R. Bersohn, and B. Katz, J. Chem. Phys. **92**, 206 (1990).
[16] J. I. Cline, C. A. Taatjes, and S. R. Leone, J. Chem. Phys. **93**, 6543 (1990).
[17] C. A. Taatjes, J. I. Cline, and S. R. Leone, J. Chem. Phys. **93**, 6554 (1990).
[18] G. E. Hall, in *Proceedings of Twelfth Combustion Research Conference*, Livermore, CA, 1990 (The Combustion Research Facility of Sandia National Laboratory), p. 122.
[19] H. L. Kim, M. A. Wickramaaratchi, X. Zheng, and G. E. Hall, J. Chem. Phys. **101**, (1994).
[20] F. J. Aoiz, M. Brouard, P. A. Enriquez, and R. J. Sayos, J. Chem. Soc., Faraday Trans. **89**, 1427 (1993).
[21] M. Brouard, S. P. Duxon, P. A. Enriquez, R. Sayos, and J. P. Simons, J. Phys. Chem. **95**, 8169 (1991).
[22] M. Brouard, S. P. Duxon, P. A. Enriquez, and J. P. Simons, J. Chem. Phys. **97**, 7414 (1992).
[23] M. Brouard, S. P. Duxon, P. A. Enriquez, and J. P. Simons, J. Chem. Soc. Faraday Trans. **89**, 1435 (1993).
[24] M. Brouard, S. P. Duxon, and J. P. Simons, Isr. J. Chem. **34**, 67 (1994).
[25] M. Baba, M. Brouard, S. P. Rayner, and J. P. Simons, Chem. Phys. Lett. **220**, 411 (1994).
[26] D. S. King, D. G. Sauder, and M. P. Casassa, J. Chem. Phys. **97**, 5919 (1992).
[27] M. P. Casassa, D. G. Sauder, and D. S. King, SPIE Proc. **1858**, (1993).
[28] N. E. Shafer, A. J. Orr-Ewing, W. R. Simpson, H. Xu, and R. N. Zare, Chem. Phys. Lett. **212**, 155 (1993).
[29] W. R. Simpson, A. J. Orr-Ewing, and R. N. Zare, Chem. Phys. Lett. **212**, 163 (1993).
[30] N. E. Shafer, H. Xu, R. P. Tuckett, M. Springer, and R. N. Zare, J. Phys. Chem. **98**, 3369 (1994).

[31] A. J. Orr-Ewing, W. R. Simpson, T. P. Rakitzis, and R. N. Zare, Isr. J. Chem. **34**, 95 (1994).
[32] N. E. Shafer-Ray, A. J. Orr-Ewing, and R. N. Zare, J. Phys. Chem. **99**, 7591 (1995).
[33] G. E. Hall, N. Sivakumar, R. Ogorzalek, G. Chawla, H.-P. Haerri, P. L. Houston, I. Burak, and H. W. Hepburn, Faraday Discuss. Chem. Soc. **82**, 13 (1986).
[34] R. Ogorzalek-Loo, G. E. Hall, H.-P. Haerri, and P. L. Houston, J. Phys. Chem. **92**, 5 (1988).
[35] R. B. Opsal, S. M. Colby, J. C. W. Wilkerson, and J. P. Reilly, in *Lasers and Mass Spectrometry*, edited by D. M. Lubman (Oxford University, Oxford, 1990), p. 490.
[36] J. F. Black and I. Powis, Chem. Phys. **125**, 375 (1988).
[37] M. Mons and I. Dimicoli, J. Chem. Phys. **90**, 4037 (1989).
[38] L. D. Waits, R. J. Horowitz, and J. A. Guest, Chem. Phys. **155**, 149 (1991).
[39] R. A. Hertz and J. A. Syage, J. Chem. Phys. **100**, 9265 (1994).
[40] H. J. Hwang and M. A. El-Sayed, Chem. Phys. Lett. **170**, 161 (1990).
[41] D. Chandler, J. Thoman, M. Janssen, and D. Parker, Chem. Phys. Lett. **156**, 151 (1989).
[42] T. Kinugawa and T. Arikawa, J. Chem. Phys. **96**, 4801 (1992).
[43] The highly visual name ''core extraction'' was brought to the authors' attention by Professor Joseph Cline (Department of Chemistry, University of Nevada at Reno) at a Western Spectroscopy Association conference (1992). Perhaps the first appearance of the name in the literature appears in Ref. 34.
[44] R. N. Dixon and H. Rieley, Chem. Phys. **137**, 307 (1989).
[45] Z. Xu, B. Koplitz, and C. Wittig, J. Chem. Phys. **90**, 2692 (1989).
[46] A. J. Orr-Ewing and R. N. Zare, Annu. Rev. Phys. Chem. **45**, 315 (1994).
[47] A. J. Orr-Ewing, W. R. Simpson, T. P. Rakitzis, S. A. Kandel, and R. N. Zare, J. Chem. Phys. (in preparation).
[48] W. W. Wiley and I. H. McLaren, Rev. Sci. Instrum. **26**, 1150 (1955).
[49] W. H. Press, B. P. Flannery, S. A. Teukolsky, and W. T. Vetterling, *Numerical Recipies* (Cambridge University, Cambridge, 1986).
[50] G. E. Busch, R. T. Mahoney, R. I. Morse, and K. R. Wilson, J. Chem. Phys. **51**, 449 (1969).
[51] Y. Matsumi, K. Tonokura, and M. Kawasaki, J. Chem. Phys. **97**, 1065 (1992).
[52] Because of a slight geometric misalignment, the photodissociation polarization data were recorded at 8° and 98° from the flight axis. This misalignment was taken into account by the data analysis program and caused only a slight decrease ($\approx$10%) in the sensitivity to the spatial anisotropy of the reactive product.
[53] It might be thought at first that measurement of the methyl product vibrational state distribution would resolve this ambiguity, but a separate measurement of that state distribution integrates over all HCl product states and does not resolve the question of methyl excitation coincident with HCl($v=1$, $J=1$) production.